18th AIAA/3AF International Space Planes and Hypersonic Systems and Technologies Conference
24 - 28 September 2012, Tours, France

AIAA 2012-5975

Analysis of a Three-Dimensional, High Pressure Ratio Scramjet Inlet with Variable Internal Contraction

Oliver M. Hohn[1] and Ali Gülhan[2]
German Aerospace Center (DLR), 51147 Cologne, Germany

We conducted an extensive experimental examination of the operational behavior of a three-dimensional scramjet inlet featuring a movable cowl to adapt the internal contraction according to the respective operation conditions. The experiments were conducted in the H2K wind tunnel of the DLR Cologne at Mach 7. The parameters investigated include different flight path angles (both angle of attack and angle of yaw), internal contraction ratio and Reynolds number. The critical internal contraction for inlet starting was found to agree well with common relations for starting of 3D-inlets. With increasing internal contraction, the inlet performance was found to improve and the inlet operated more stable. It was successfully tested for angles of attack up to ± 6° and angles of yaw up to 6°. Reynolds-Number had rather small effects on the performance and starting behavior of the inlet. Infrared-thermography also gave some insight into the flow structure in the external part of the inlet.

Nomenclature

A	=	area
C_p	=	specific heat capacity at constant pressure
C_v	=	specific heat capacity at constant volume
CR	=	contraction ratio $CR = A_{capture} / A_{th}$
I	=	internal contraction ratio $I = A_{lip} / A_{th}$
M	=	Mach number
$\dot{m}$	=	mass flow
MCR	=	mass capture ratio
p	=	pressure
R	=	specific gas constant for air, $R = 287.15$ J kg^{-1} K^{-1}
Re	=	unit Reynolds number
St	=	Stanton number
T	=	temperature
t	=	time
α	=	heat transfer coefficient, calibration factor or angle of attack
β	=	angle of yaw
γ	=	ratio of specific heats
Δ	=	throttle degree
η	=	kinetic energy efficiency
λ	=	heat conductivity
π	=	total pressure ratio
Π	=	static pressure ratio
ρ	=	density

Subscripts:

D	=	throttle

[1]Research Scientist, Supersonic and Hypersonic Technology Department, Institute of Aerodynamics and Flow Technology, German Aerospace Center (DLR), Linder Höhe, 51147 Cologne, Germany. AIAA Member.
[2] Head of Department, Supersonic and Hypersonic Technology Department, Institute of Aerodynamics and Flow Technology, German Aerospace Center (DLR), Linder Höhe, 51147 Cologne, Germany. AIAA Member.

rec = recovery
st = static
t0 = wind tunnel total conditions
∞ = wind tunnel free stream conditions

I. Introduction

ALTHOUGH the research on Scramjet-engines has been a major focus in the development of advanced high-speed propulsion systems for several decades [1], [2], in recent years especially the advances in flight testing have sparked a renewed interest in this field of science and triggered several new research projects such as HyShot [3] and the consequent Scramspace [4], [5] and HiFIRE [6], [7] programs, the Hyper-X/X-43 [8], [9] and X-51 [10] projects, or LAPCAT [11], [12] and LEA [13], [14]. The Supersonic and Hypersonic Technology Department of the German Aerospace Center in Cologne also has a long history of research in high-speed propulsion, especially in inlet testing, as the experimental facilities allow for the aerodynamical testing of various inlet types over wide Mach number ranges. The present study is part of the continuous efforts in this research area and is integrated in the research training group GRK 1095/2 of the German Research Foundation in which a considerable part of scramjet research activities in Germany is concentrated [15], [16].

The key features of a scramjet propulsion system are that is does not use a mechanical compression system to reach the flow conditions required in the combustion chamber but merely the deceleration of the flow in the inlet section, and, in contrast to a regular ramjet, that combustion takes place at supersonic speeds. This poses strong requirements on the design of the inlet as it has the task of supplying the airflow at the conditions required for supersonic combustion to take place and makes it a very critical system component. The quality at which the inlet realizes this task, is crucial to the overall performance of the Scramjet [17].

Although there has been some research on three-dimensional inlets in the past, especially on sidewall-compression inlets [18–20] or axisymmetric configurations [17], [21] most research on hypersonic inlets has been on two-dimensional inlets [22–24]. Also the inlets of several flight experiments [10], [25], and other research projects [26], [27] are two-dimensional. However, recent developments focus more on 3D-configurations. Heiser and Pratt [1] list several advantages of three-dimensional designs. The compression in both vertical and horizontal planes, allows for a more compact and lighter design. Ramp angles can be smaller, resulting in weaker shocks, lower total pressure losses and less shock-induced incipient separation. Furthermore advances in design techniques such as streamline tracing [28–30] enable more possibilities regarding the engine configuration.

The inlet analyzed in the current paper was designed according to requirements of a flight experiment with a parabolic reentry flight, where, like with HyShot, Scramjet operation is achieved in a certain corridor during reentry. According to trajectory calculations, this corridor would be in an altitude between 30 and 25 km, at flight Mach numbers between 7 and 8 [31]. A combustion chamber with a central strut injector and staged combustion [32] was adopted but modified to allow for higher fuel ratios [33].

Like HyShot, the proposed flight configuration does not feature a forebody. Consequently, the inlet needs to have a high static pressure ratio of about $\Pi_{st} \approx 45$ (and correspondingly large contraction around $CR \approx$ 8-8.5), in order to achieve the conditions required for supersonic combustion (static pressure of about 50 kPa and static temperature of 1000 K) [3], [34], [35]. A 3D-inlet with a single ramp and straight converging sidewalls was found best suited for this task, as specified in section II. The shock structures in this kind of geometry, especially the interaction of ramp and sidewall shocks in the corners, cause a very complex flow structure which is described in detail by Goonko [36] or Nguyen [37]. Previous investigations with an originally two-dimensional inlet which was modified with inserts for additional sidewall compression showed the impact this interaction can have on the flowfield and overall performance of the inlet [38]. To reduce these effects, radiuses were applied to the corners.

Due the geometrical constraints and the wish to minimize spillage (and consequent losses) starting of the inlet becomes very problematic. The internal contraction ratio I of the inlet would be way above the Kantrowitz criterion [39] for self-starting of the inlet. Even though this is not a strong criterion, as several examples from the literature suggest that self-starting of inlets is also possible at internal contraction ratios above the Kantrowitz limit [17], [38], [40], the experience from these and other investigations [41], [42] strongly suggest that the inlet under investigation would not be starting in its design point. In order to still be able to achieve optimal inlet performance, a movable cowl as starting mechanism was integrated. It also gives the opportunity to investigate the inlet at different internal contraction ratios and adapt it to off-design conditions such as angle of attack and different Mach numbers.

This paper presents the results of the first measurement campaign with this inlet. It was performed at a fixed Mach number with at two different flow conditions to investigate the influence of Reynolds-number variation, as described in the next section. For the examination of different flight path angles, angles of attack up to $\alpha = \pm 6°$ and

angles of yaw up to $\beta = 5°$. The influence of the internal contraction ratio was analyzed as well and the critical internal contraction with regard to inlet starting was determined. Furthermore, IR-measurements of the external part of the inlet were conducted to give some insight into the flow structure.

II. Experimental Setup

A. Wind Tunnel and Test Conditions

All of the experiments presented in this paper have been conducted in the Hypersonic Windtunnel H2K at the German Aerospace Centre in Cologne. This facility is a blow down wind tunnel using contoured axisymmetric nozzles for fixed Mach numbers with an exit diameter of 600 mm. It is designed to simulate Mach numbers of 5.3, 6, 7, 8.7 and 11.2 at Reynolds numbers in the range of $2.5 - 20 \cdot 10^6$ m^{-1} [43]. Depending on the flow condition, test durations of up to 30 s can be achieved. A sketch of the H2K is shown in Figure 1.

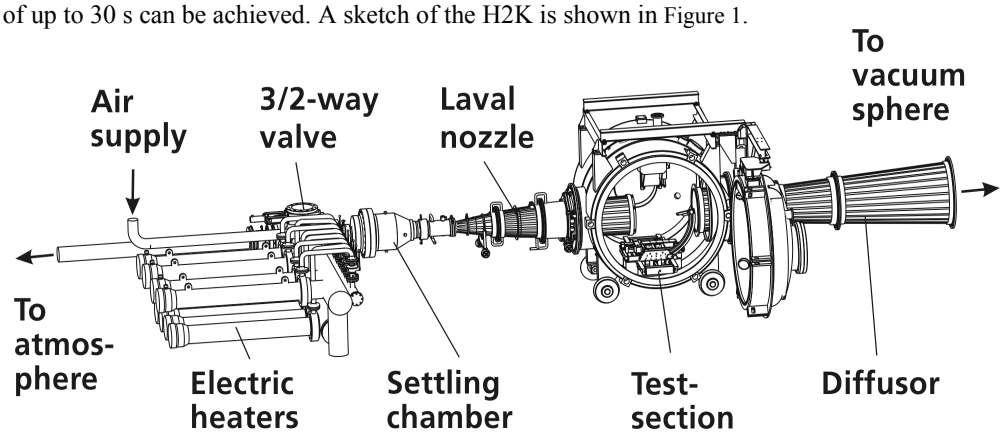

Figure 1: Schematic drawing of H2K

The test conditions used are displayed in Table 1. These were chosen considering Reynolds number similarity for a Mach 7 flight of a full scale model for flight altitudes of 30 km (cond. 1) and 25 km (cond. 2) respectively. The test series was performed at a nominal Mach number of 7. However, the actual Mach number is influenced by the boundary layer in the nozzle which depends on the Reynolds number. Therefore the actual freestream Mach number deviates slightly from the nominal one, with 7.02 for condition 1 and 7.06 for condition 2. The variation of the Mach number over the cross-section of the core flow region is less than 0.5%. Variation of total temperature during the tests was about $\Delta T_{t0} = \pm 11$ K or 1.6% for both conditions, and for total pressure about $\Delta p_{t0} = \pm 8$ kPa or 1% for condition 1 and $\Delta p_{t0} = \pm 20$ kPa or 1.1% for condition 2.

Flow parameter	Cond. 1	Cond. 2
freestream Mach number M_∞, -	7.02 ± 0.04	7.06 ± 0.04
total temperature T_{t0}, K	700 ± 11	700 ± 11
total pressure p_{t0}, kPa	790 ± 8	1750 ± 20
freestream pressure p_∞, Pa	191 ± 3	423 ± 8
freestream temperature T_∞, K	64.8 ± 1	64.8 ± 1
unit Reynolds number $Re_{\infty,m}$, m^{-1}	$(2.6 \pm 0.1) \cdot 10^6$	$(5.7 \pm 0.2) \cdot 10^6$

Table 1: Wind-tunnel conditions

B. Inlet Model

Figures 3 through 5 show an image of the inlet model used in the current measurement campaign mounted in the H2K test section as well as schematic sketches. Overall, the model is 750 mm long, with the defined interface of inlet/isolator and the combustion chamber at $x = 650$ mm.

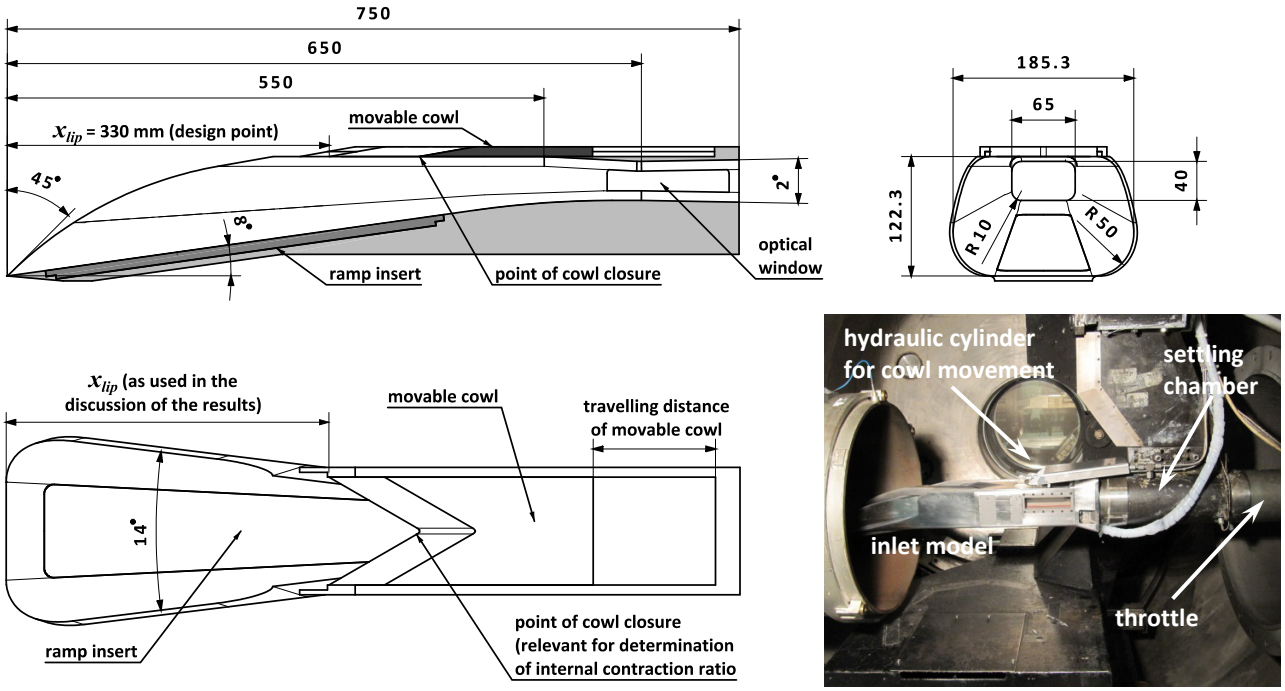

Figure 2: Schematic drawings of the inlet model: cut and fronf views (top left and right) top view (bottom left) and photo of the model mounted in the test chamber of H2K (bottom right).

Downstream of this location, the top and bottom walls are divergent by 1° each. The ramp angle is 8° and the sidewall angles are 7° each, giving a total sidewall convergence angle of 14°. The fixed part of the cowl starts at 550 mm with an angle of 3°. The movable part can be shifted by Δx_{lip} = 150 mm so that the lip position can be varied in between x_{lip} = 300 and 450 mm, as indicated in Figure 3. Thus, it is possible to modify the internal contraction ratio in the range of I = 1.3 and 2.7. The design point for shock-on-lip condition is at x_{lip} = 330 mm. The lip of the cowl is V-shaped in order to best adapt to the structures of the ramp and sidewall shocks although of course it is not possible to exactly match the shape of shock structures. A part of the bottom surface of the external ramp can be replaced by an insert which is suitable for IR-measurements. The capture area of the inlet is about A_{ref} = 0.02 m^2, with a maximum width of 185.3 mm and maximum height of 122.3 mm. The throat area at the interface of inlet and combustion chamber at x = 650 mm is A_{th} = 2.51 · 10^{-3} m^2, giving an overall contraction ratio $CR = A_{ref}/A_{th}$ = 8.12.

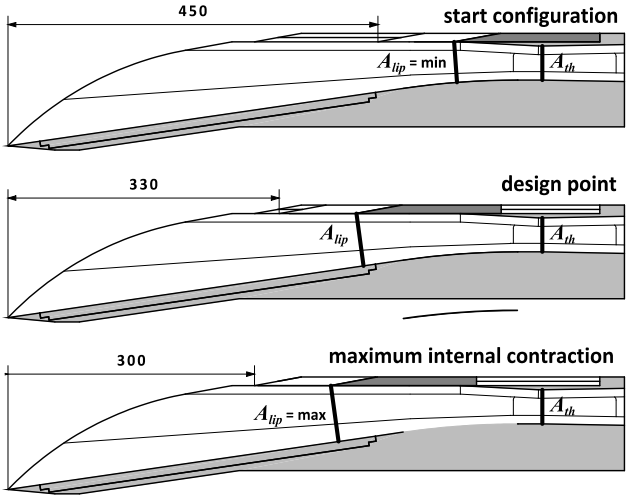

Figure 3: Model with cowl in start (top), design (middle) and maximum (bottom) positions

III. Measurement Techniques

A. Pressure Measurements and Calculation of Mach-Number

Overall, the inlet model is equipped with 55 wall pressure tabs. 30 of these are located along the centerline of the lower wall, 9 on the fixed part of the upper wall and 4 on the moveable cowl. Furthermore, there are two cross-sections, at x = 500 mm and x = 590 mm with circumferential distribution of 6 pressure tabs each. The locations of the pressure tabs along the centerline and around those two cross-sections are displayed in Figure 4.

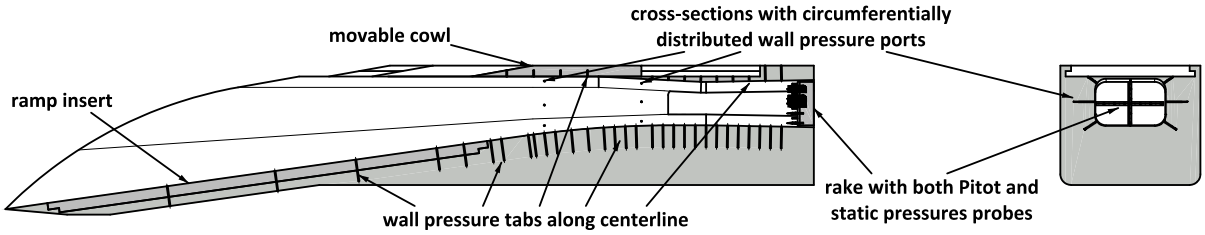

Figure 4: Distribution of pressure measurement tabs

A cross-shaped pressure measurement rake incorporating both Pitot pressure tubes as well as static pressure probes is used to determine Pitot and static pressure distribution at the downstream end of the inlet model (at x = 720 mm). The static pressure probes are designed according to Pinckney [44–46], and enable the measurement of the static pressure very close to the tip of the probe. The Pitot and static pressure tubes are arranged in an alternating fashion. Over the span wise direction the probes on one side of the centerline are in reversed order as on the other side. Assuming a symmetrical flowfield in the inlet, this enables measuring both static and Pitot pressure at the same location, i.e. at the same distance from the center plane. The measurements of the wall pressure ports distributed around the two cross-sections mentioned above suggest that this assumption is valid as the deviation of measurements on the left and the right side were within 3%. This allows for a quite accurate determination of static and Pitot pressure profiles as well as Mach number distributions over the width of the inlet, as the Mach number at one point can be calculated from the ratio of Pitot and static pressure.

If the flow is supersonic, the ratio Pitot and static pressure is $p_{Pitot}/p_{st} \leq 1.8939$ and the Mach number can be determined by equation 1 [47]:

$$M_{Pitot} = \sqrt{\frac{2}{\gamma-1}\left[\left(\frac{p_{Pitot}}{p_{st}}\right)^{\frac{\gamma-1}{\gamma}} - 1\right]} \tag{1}$$

In the case when $p_{Pitot}/p_{st} > 1.8939$ the flow is subsonic and the Mach number has to be calculated iteratively from equation 2 [47]:

$$\frac{p_{Pitot}}{p_{st}} = \left(\frac{(\gamma+1)^2 \cdot M_{Pitot}^2}{4\gamma \cdot M_{Pitot}^2 - 2(\gamma-1)}\right)^{\frac{\gamma}{\gamma-1}} \cdot \frac{1-\gamma+2\gamma \cdot M_{Pitot}^2}{\gamma+1} \tag{2}$$

A commercial Pressure Systems Inc. 8400 system [48] was used for the pressure measurements. The accuracies in the determination of the pressure ratios have been calculated to range from ±3.8-5.6% for static and ±3.4-3.8% for Pitot pressures. For the Mach number derivation, the horizontal and vertical parts of the Pitot rake have to be regarded separately. As mentioned above, the Pitot rake enables the determination of both static and Pitot pressure at the same distance from the center plane. Regarding a ±3% deviation in the pressure measurement due to small asymmetries of the flowfield results in a certainty of the Mach number calculation of about ±2%. For the vertical profiles, accuracy is much lower, as the pressure values have to be interpolated between the nearest pressure probes. Assuming a 10% variation of the static pressure at a Pitot tube from the interpolated value, it gives an accuracy of around ±6% for the Mach number determination [49]. For those experiments, where an angle of yaw was applied, the flowfield naturally is not symmetrical anymore, and the pressures had to be interpolated for the horizontal profiles as well, with the consequent reduced accuracy.

Using the Mach number results, the total pressure the location of the probes can be calculated as well as the total pressure recovery π and the kinetic energy efficiency η_{ke} of the inlet according to equations 3 and 4. The accuracy of these values is around ±25% and ±2.5%, respectively [50].

$$\pi = \frac{p_{t,Pitot}}{p_{t0}} \tag{3}$$

$$\eta_{ke} = 1 - \frac{2}{(\gamma-1)\cdot M_\infty^2} \cdot \left[\left(\frac{1}{\pi}\right)^{\frac{\gamma}{\gamma-1}} - 1\right] \tag{4}$$

B. Mass Flow Determination

During the tests, the inlet is mounted on a conical throttle, which is used to simulate the backpressure of the combustion chamber by varying the throttle exit diameter with a hydraulic cylinder. That way, during one test run, full performance mappings (so called throttle curves) can be recorded. At the start, the throttle is open, and no back-

pressure is applied. Then, the throttle is steadily moved, increasing the backpressure up to the point of inlet unstart. Besides, the throttle also serves as a mass flow meter. Assuming a one-dimensional flow and sonic condition in the throat of the throttle, the mass flow can be calculated with the procedure from Triesch and Krohn [51].

The mass capture ratio *MCR* of the inlet is defined as

$$MCR = \frac{\dot{m}_{inlet,exit}}{\dot{m}_0} \tag{5}$$

The smallest cross-section area of the throttle, designated by index 4, is calculated with the position of the conical and the geometric dimensions of the throttle by

$$A_{sc} = \pi \cdot s \cdot (r_H + r_4) \tag{6}$$

The Mach number in the settling chamber before the throttle (position 3) can then be determined by iteratively solving equation 5:

$$\frac{A_{tt}}{A_{st}} = \frac{1}{M_{sc}} \cdot \left(\frac{2+(\gamma-1)\cdot M_{sc}}{\gamma-1}\right)^{\frac{\gamma+1}{2(\gamma-1)}} \tag{7}$$

Using the static pressure measured before the throttle (at position 3), the mass flow can be calculated with the total temperature T_{t0} and M_{D3} by

$$\dot{m}_{inlet} = K \cdot A_{tt} \cdot M_{sc} \cdot \frac{p_{sc}}{\sqrt{R \cdot T_{t0}}} \cdot \sqrt{\gamma \cdot \left(1 + \frac{\gamma-1}{2} M_{sc}^2\right)} \tag{8}$$

where *K* is a calibration factor determined by calibrating the device according to DIN-1952 [52]. In the region of interest, the values of this factor vary between $0.99 < K < 1.02$. The static pressure p_{D3} is taken as the average value of four pressure ports located around the settling chamber of the throttle. With the mass flow $\dot{m}_0$ going through the capture area A_0 of the inlet, which can be calculated by the free stream conditions of the wind tunnel, the mass flow ratio according to equation 5 can then be determined. The accuracy of this method is in the range of ±2.4% [50].

C. Optical Diagnostics

1. Schlieren images

A coincidence Schlieren optics system is installed at the H2K for flow visualization and surveillance of the experiments. The inlet model only has optical access to the throat section downstream of the converging part of the sidewalls. Therefore, only limited insight could be gained from the Schlieren images. Furthermore, the test condition with a rather high total temperature causes the windows to heat up quite strongly which in turn causes blackening of the Schlieren images.

2. Wall Heat Flux Evaluation

The determination of wall heat fluxes is substantial in scramjet engine design, especially for the selection of cooling mechanisms as well as materials. In this investigation, heat fluxes of the external ramps have been determined. A part of the bottom ramp of the inlet can be replaced by an insert made of polyether-ether-ketone, a thermoplastic with a very low thermal conductivity which serves as a measurement surface.

During the experiments, the surface temperature distribution of this insert is recorded with an infrared camera [53]. Assuming that lateral heat fluxes can be neglected due the low thermal conductivity of the material used the heat fluxes can be determined by using the recorded surface temperature data as the boundary condition for the thermal energy balance normal to the wall:

$$\rho(T) \cdot c(T) \frac{\partial T}{\partial t} = \frac{\partial}{\partial n}\left(\lambda(T) \frac{\partial T}{\partial n}\right) \tag{10}$$

Accounting for temperature dependent material properties, this transforms into the nonlinear one-dimensional heat equation

$$\frac{\partial T}{\partial n} = a(T) \cdot \frac{\partial^2 T}{\partial n^2} + b(T) \cdot \left(\frac{\partial T}{\partial n}\right)^2 \tag{11}$$

with the thermal diffusivity

$$a(T) = \frac{\lambda(T)}{\rho(T) \cdot c(T)} \tag{12}$$

and

$$b(T) = \frac{\frac{d\lambda(T)}{dT}}{\rho(T) \cdot c(T)} \tag{13}$$

The low thermal conductivity of polyether-ether-ketone temperature ensures that gradients normal to the surface are dominant and lateral heat flux are kept minimal and thus can be neglected. This allows for this 1-D approach to be valid. Equation 11 is then solved by an explicit finite difference scheme to calculate the temperature gradient normal to the wall and the heat fluxes. A detailed description of this procedure can be found in [54]. Once the convective wall heat fluxes have been determined, the dimensionless Stanton can be determined by

$$St = \frac{\dot{q}_{conv}}{\rho_\infty \cdot u_\infty \cdot c_{p,air} \cdot (T_{rec} - T_w)} \tag{12}$$

where the recovery temperature T_{rec} is defined by

$$T_{rec} = \left(1 + r\frac{\gamma+1}{2} \cdot M_\infty^2\right) \cdot T_\infty \tag{13}$$

For the recovery factor, the common value of r = 0.9 is used.

Regarding the accuracy, the manufacturer reports a maximum error for the temperature measurement of the IR-camera of ±2 K or 2%, which ever value is higher [53]. An analysis of all uncertainties of this procedure resulted in maximum errors of ±5% for the heat fluxes and ±20% for the Stanton number.

IV. Results

A. Critical Internal Contraction Ratio

The movable cowl as the starting mechanism can be used to determine the critical internal contraction ratio I_{crit} for self-starting of the intake by reversing the test procedure. At the start of the experiment, the cowl is in its most upstream position (at x = 300 mm), the internal contraction is maximal and the inlet flow does not establish upon the start of the windtunnel run. Then, the cowl is slowly moved back, decreasing the internal contraction until at one point, the inlet flow suddenly builds up, as displayed in Figure 5, which shows Schlieren images of the unstarted (top) and started (bottom) cases, in combination with the assumed flow structure based on van Wie [17] and the static pressure distribution on the ramp, which is also included in the image (red line). At the start of the windtunnel, the internal flow does not built up, shown in the upper image which shows the situation just before the inlet starts (x_{lip} = 359 mm). Presumably, a large separation bubble forms on the external ramp, creating fans of shock and expansion waves, just slightly visible in the Schlieren image but also indicated by the gradual pressure rise. The flow in the internal part is blocked and completely subsonic whereas the spillage mass flow is at very low supersonic velocities,

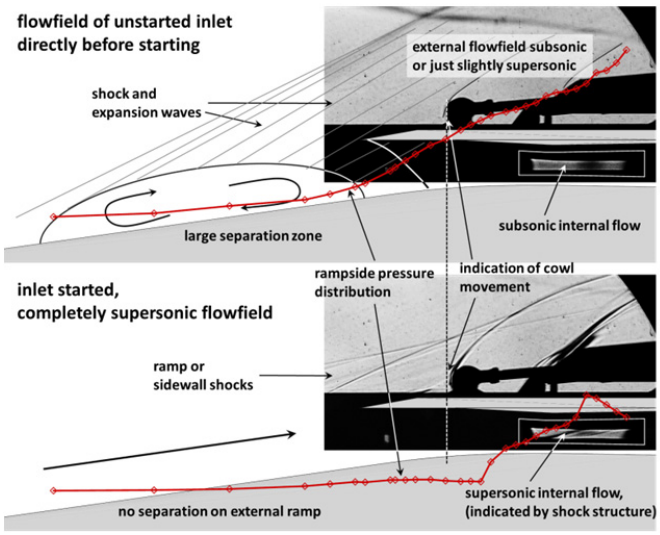

Figure 5: flow structure of starting process

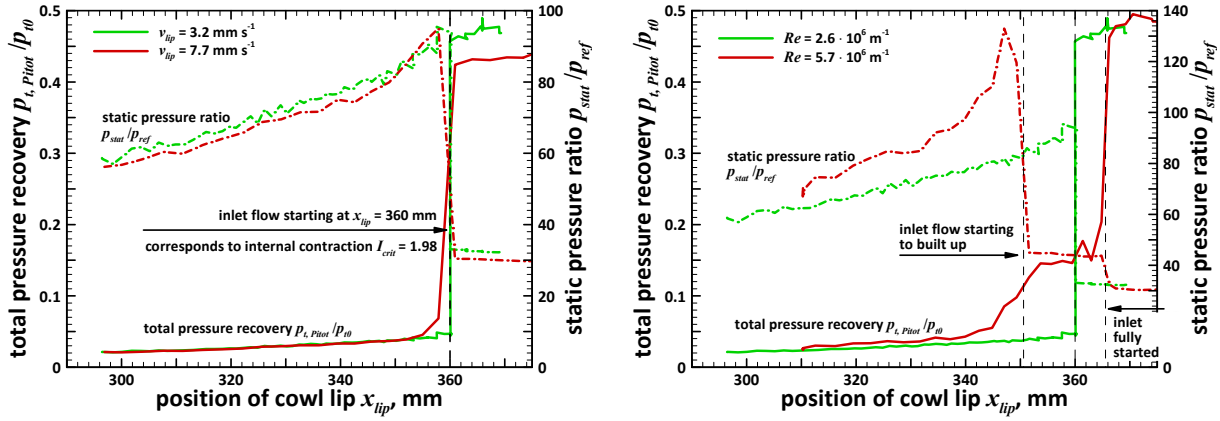

Figure 6: critical internal contraction for cond. 1 (left) and comparison of starting for cond. 1 and 2 (right)

as the very weak shocks around the cowl suggest (they were highlighted in the image as otherwise they are barely recognizable). The lower picture shows the situation directly after the built-up of the inlet flow. As indicated, the cowl is moved downstream just 1 mm more, the flow suddenly builds up: the separation bubble is swallowed by the inlet, and the supersonic internal flow is established, which is visible by both the pressure distribution as well as the shock structures visible in the Schlieren image (both in the internal and the external flowfield). The determination of the exact lip position and internal contraction ratio of the point of inlet start is determined from the pressure measurements. When the flow starts, the static pressure drops and total pressure rises sharply, as illustrated in Figure 6 (left image).

The critical internal contraction of I_{crit} = 1.98 fits very well with results from other investigations [40]. The figure also shows the comparison of two different cowl velocities, in order to ensure that the process is not influenced by hysteresis effects. At the higher velocity of v_{lip} = 7.7 mm s^{-1}, it is not possible to determine the position as accurately as for v_{lip} = 3.2 mm s^{-1} but the results are sufficient to conclude that it does not play a considerable part.

Figure 6 (right) shows the comparison of the starting behavior of the two conditions used in the test series. It shows that for cond. 2, the intake flow does not start spontaneously at one point, but at first, at a higher internal contraction ratio of about I = 2.2 (corresponding to a lip position of x_{lip} = 345 mm), only partially builds up, but only at an internal contraction ratio lower than in the case of condition 1, the flow is fully established, at around x_{lip} = 366 mm or $I_{crit,2}$ = 1.9. The starting limits for both conditions are displayed in Figure 7 in relation to the Kantrowitz limit [39] and an empirical relation found by Sun [40], which correlates data from various kinds of investigations on 3D-inlets.

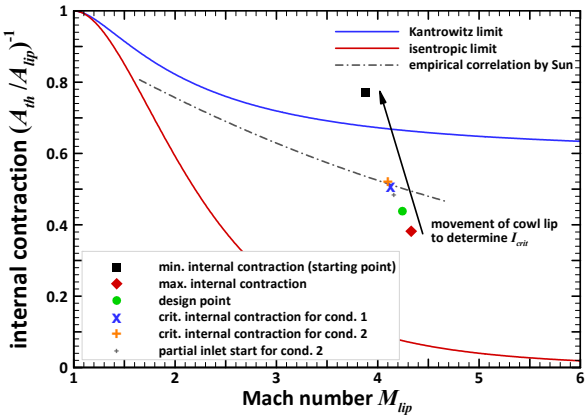

Figure 7: comparison of starting limits

B. Comparison of different internal contraction ratios

To investigate the influence of the internal contraction and determine the cowl position with the best inlet performance, several windtunnel runs where, after inlet starting, the cowl was moved to a defined position and then a throttle curve was recorded.

The total pressure recovery and the static pressure ratio for these tests are shown in Figure 8. At high throttle degrees (i.e. when $\Delta \geq 0.19$, the backpressure from the throttle does not affect the inlet yet) the pressure ratio is about Π = 41 and is not influenced by the lip position. For the pressure recovery, there are some differences for the various lip positions, with values in the range of π = 0.44 for x_{lip} = 320 mm and 0.475 x_{lip} = 340 mm, or about 7%.

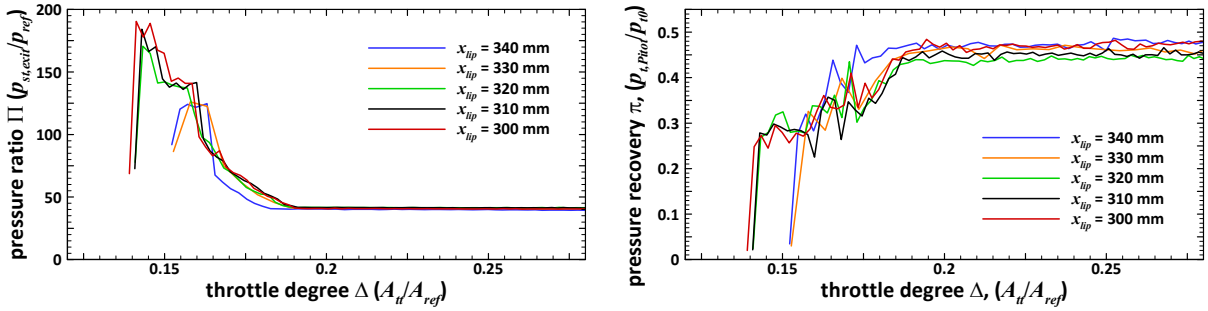

Figure 8: static pressure ratio (left) and total pressure recovery for different lip positions

At high backpressure, i.e. at low throttle degrees, shows two distinct patterns are visible. For $x_{lip} \geq$ 330 mm, the maximum pressure ratio is about Π = 120 to 125 and the inlet unstarts at throttle degrees of about $\Delta \approx 0.155$. In the cases with higher internal contraction, for $x_{lip} \leq$ 320 mm, the inlet still operated at pressure ratios of up to Π = 170 for x_{lip} = 320 mm and Π = 190 for x_{lip} = 300 mm, and the point of inlet unstart is around $\Delta \approx 0.14$. This is also true for other lip positions which, for better clarity, are not presented in the figures.

The reason lies in different the flow topology of these two cases which is sketched in Figure 9. For x_{lip} ≥ 330 mm, the ramp shock misses the cowl, whereas for the other configurations, it goes underneath the cowl causing the boundary layer on the cowl surface to separate, which extends up to the lip so that the corresponding separation shock sits directly at the lip and interacts with the ramp shock. Apparently, this flow structure is more stable to the backpressure. The separation bubble seems to function like a buffer. In the other case the rising backpressure causes the cowl shock to jump out of the inlet and cause unstart much sooner. In a way, the whole internal part acts as the isolator, even the converging part upstream of the throat section. Consequently, the inlet operates most stable when the lip is in it most upstream position. And, as Figure 8 and Table 2 show, this configuration also has the best performance.

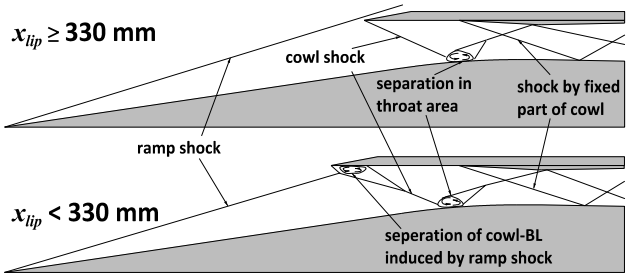

Figure 9: centerline flow topology for different lip positions

The flow structure apparently is not influenced by the lip position when the ramp shock goes underneath the cowl, as the wall pressure distribution in Figure 10 suggests. For x_{lip} ≥ 330 mm you can see the point of the pressure rise at the bottom wall, where the cowl shock hits the ramp surface, move upstream according to the change in lip position. For x_{lip} ≤ 320 mm this is not the case anymore and for x_{lip} = 310 and 300 mm the lines are nearly identical.

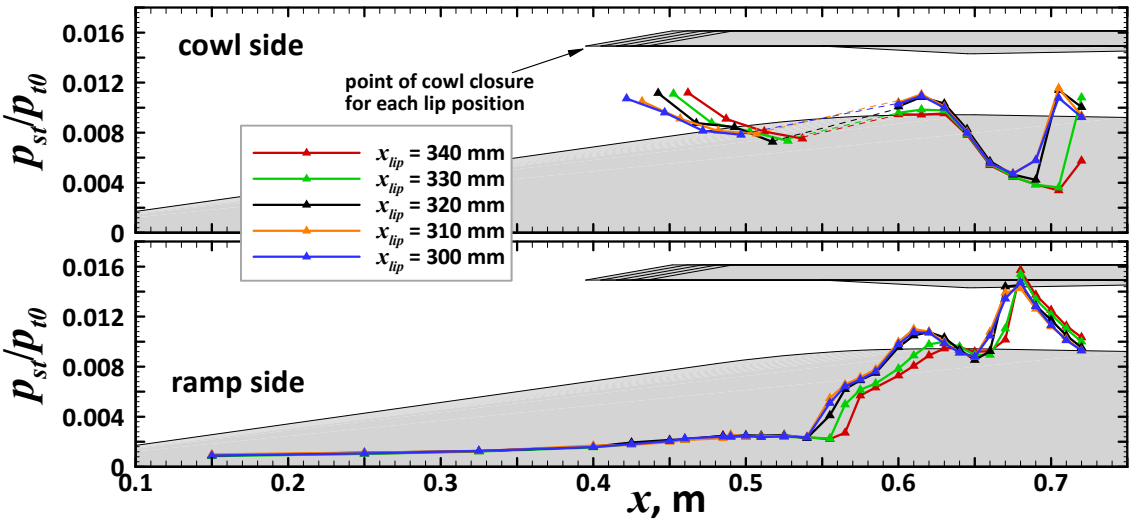

Figure 10: wall pressure distribution for different lip positions with no backpressure applied

For all lip positions, the wall pressure distributions reflect the expected flow topology at the center plane. At the point of the first strong pressure rise at the lower wall (around x = 0.54-0.56 m), the cowl shocks hits the ramp. The point of the second pressure rise is where the shock emanating from the edge of the fixed part of the cowl interacts with the ramp. This shock also causes the pressure rise on the upper wall in between the movable and fixed part of the cowl (indicated by the dashed line). Further downstream, pressure drops due to the expansion of the corner where the fixed cowl transitions to the throat and later to the diverging isolator section. The jump in pressure just before the downstream end marks the interaction of the reflected cowl shock with the upper wall. For x_{lip} = 340 mm, the shock apparently hits the cowl surface only downstream of the last pressure port.

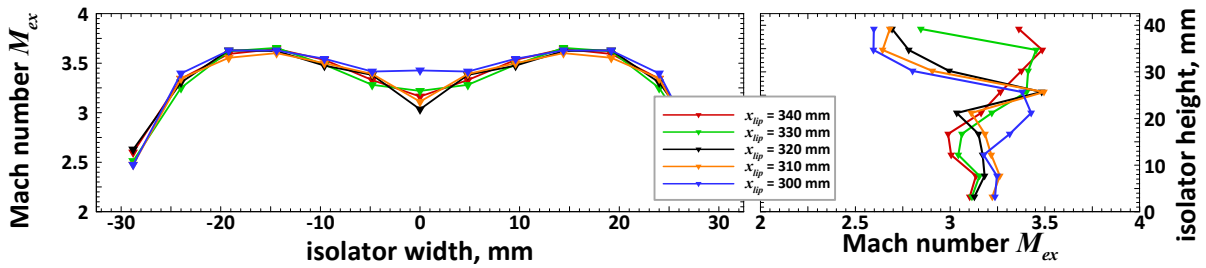

Figure 11: Horizontal (left) and vertical (right) Mach number profiles for different lip positions

Because of this, only a little pressure rise is recorded, although it is expected to be of the same magnitude than in the other cases. This is also supported by the Mach number profiles shown in Figure 11, as the Mach number in the upper half of the isolator shows the location of the cowl shock structure. For x_{lip} = 300, 310 and 320 mm, the shock, reflected from the upper wall, passes in between the third and fourth point from the top, causing the strong change in Mach number. For x_{lip} = 330 mm, it is moved downstream so that the shock passes in between the first and second location, and for x_{lip} = 340 mm, it seems be located in between the wall and the top Pitot probe. In the bottom half, the flow structure is very much influenced by the shock from the fixed part of the cowl, and thus the influence of the lip position is not as distinct. It is only influenced by the shock-shock-interaction with the cowl-shock-structure, as well as changes in the boundary layer and consequently the shock-boundary layer interaction. Regarding the horizontal profile, the lip position hardly has any influence, as both shocks always pass either above or below the horizontal rake for all configurations. Regarding the horizontal Mach number profiles, it is very interesting to note that, apart from the points closest to the walls, the flow seems to be quite uniform, especially for x_{lip} = 300 mm. There are no sudden changes in the Mach number profiles, which suggests that the sidewall shocks do not propagate into the isolator section. However, the drop in Mach number at the centerplane for most configurations could be a sign for the existence of the vortices.

Figures 12 and 13 show the changes in wall pressure and Mach number distributions for x_{lip} = 300 mm when the backpressure imposed by the throttle is increased during the test run. The backpressure propagates upstream through the ramp side boundary layer, inducing a shock train (at the beginning it is only a single oblique shock) which moves upstream as the backpressure is further increased. This can also be observed by the Mach number profile over the isolator height. The backpressure only starts to influence the cowl side pressure distribution when this shock has moved so far upstream that it hits the cowl surface, which occurs at a backpressure ratio of 74. When the backpressure is further increased, a very sudden change takes place: the flow structure completely changes, causing a jump in the backpressure ratio from 98 to 141. The shock train now starts at the upper wall, at about x = 0.64 m. Downstream of this point, the flow in the upper section is subsonic, and probably the boundary layer separates as well.

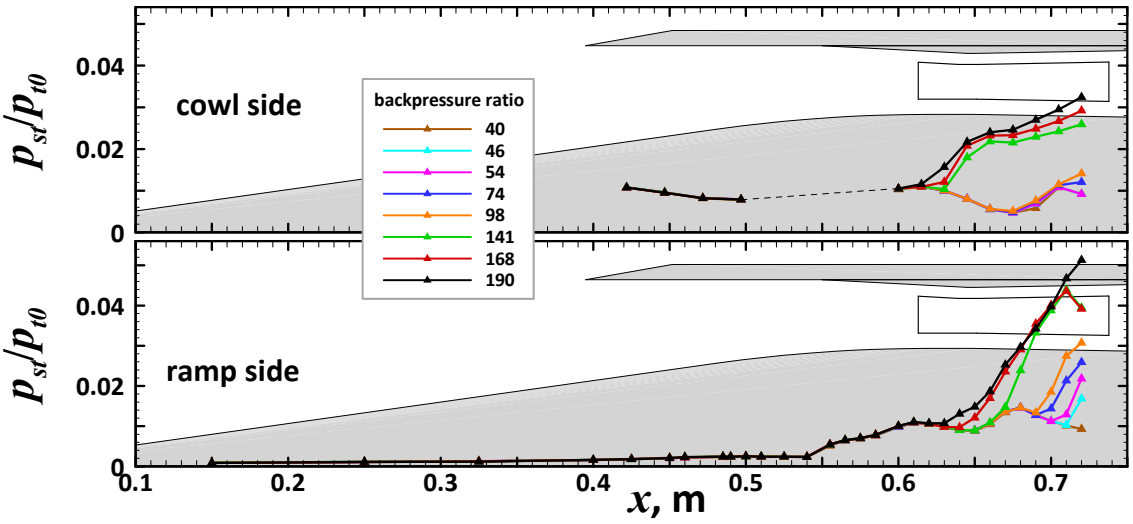

Figure 12: wall pressure distribution for different backpressure ratios for x_{lip} 300 mm

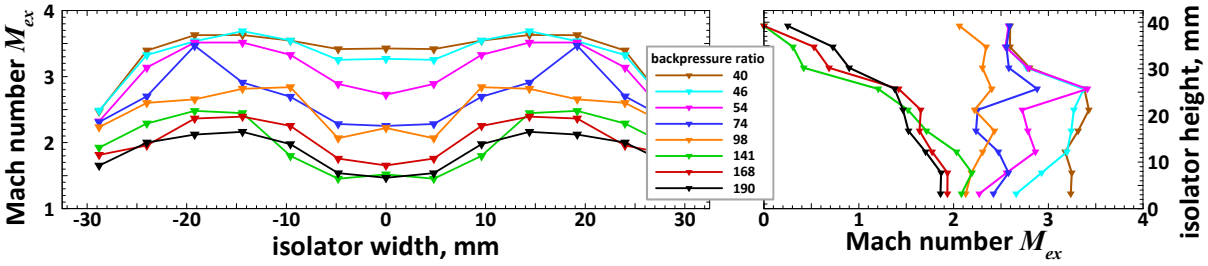

Figure 13: Mach number profiles for different backpressure ratios for x_{lip} = 300 mm

In the center and lower parts of the isolator, the flow remains supersonic, as both the horizontal and vertical Mach number profiles show, as well as the wall pressure distribution, which also indicates the structure of the shock train. As the backpressure is further increased the shock train moves slightly upstream and becomes stronger until at a backpressure ratio of just over 190, the cowl shock pops out of the inlet and the inlet flow unstarts.

The following Table 2 summarizes the performance parameters for the configurations with different internal contractions (also for those omitted in the previous discussion for better clarity). Overall, the configuration with maximum internal contraction performs best and operates most stable.

x_{lip}, *mm*	*I*	*MCR*	π_t	Π_{st}	η_{ke}
300	2,62	0,97	0,47	41,58	0,98
305	2,56	0,96	0,45	41,40	0,97
310	2,50	0,97	0,45	41,44	0,97
315	2,45	0,95	0,43	41,58	0,97
320	2,39	0,95	0,44	41,51	0,97
325	2,34	0,94	0,41	41,66	0,97
330	2,28	0,92	0,46	40,96	0,98
335	2,23	0,87	0,46	41,31	0,97
340	2,17	0,90	0,47	39,93	0,47
362	1,97	0,85	0,47	38,90	0,98
365	1,92	0,84	0,49	38,70	0,98

Table 2: performance parameters for various internal contraction ratios

C. Influence of Flight Path Angles

For the analysis of the influence that both angle of attack and yaw have on the inlet performance, only the design configuration (x_{lip} = 330 mm) and the configuration with the maximum internal contraction (x_{lip} = 300 mm), were used. Since this inlet is designed for a parabolic flight experiment, rather large flight path angles of α = ±3° and ±6°, where positive α is in clockwise direction, and β = 3° and 6° were considered.

1. Angle of Attack

During the experiments, the angle of attack was set up with a hydraulic positioning device. At the start of wind tunnel, the model was in the starting configuration and the angle was at α = 0°. After the start of the windtunnel, both the lip position and angle were set up, and a throttle curve was recorded. Figure 14 presents the pressure ratio and recovery for these two configurations for the various angles of attack. As expected, in the unthrottled case the pressure ratio decreases for positive angle of attack, as the ramp angle with respect to the free stream becomes smaller resulting in lower compression. Vice versa, it becomes larger for negative angle of attack, causing a higher pressure ratio. For all values of α, the configuration with maximum internal contraction delivers a higher pressure ratio than the design configuration. Also the maximum pressure ratio, at which the inlet can still operate in each case, is larger for this configuration, and the throttle degree, at which the inlet unstarts, is lower. This is also true for the case of negative α, where performance seems to be better in the design configuration. However, the pressure recovery and mass flow measurements (which are not presented) show strong oscillations which indicate inlet buzzing. For all other configurations, the inlet performs stable up to the point of inlet unstart. The configuration with maximum internal contraction, delivers better performance and more stable operation than the design case.

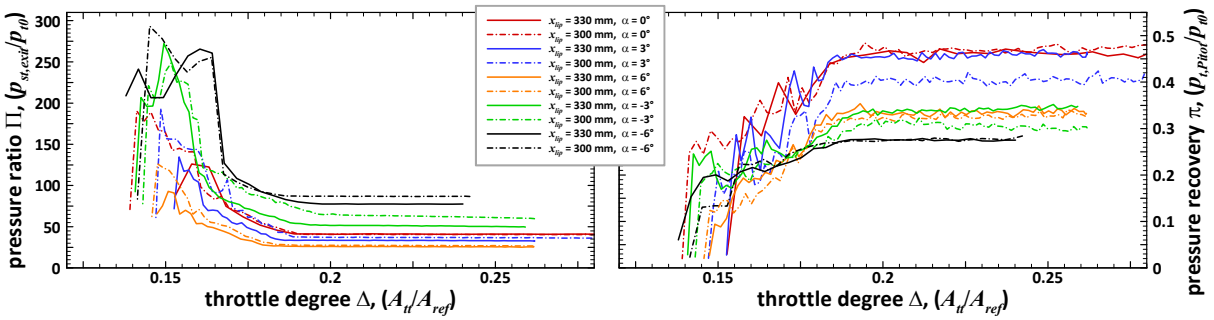

Figure 14: Static pressure ratio and total pressure recovery for different angles of attack

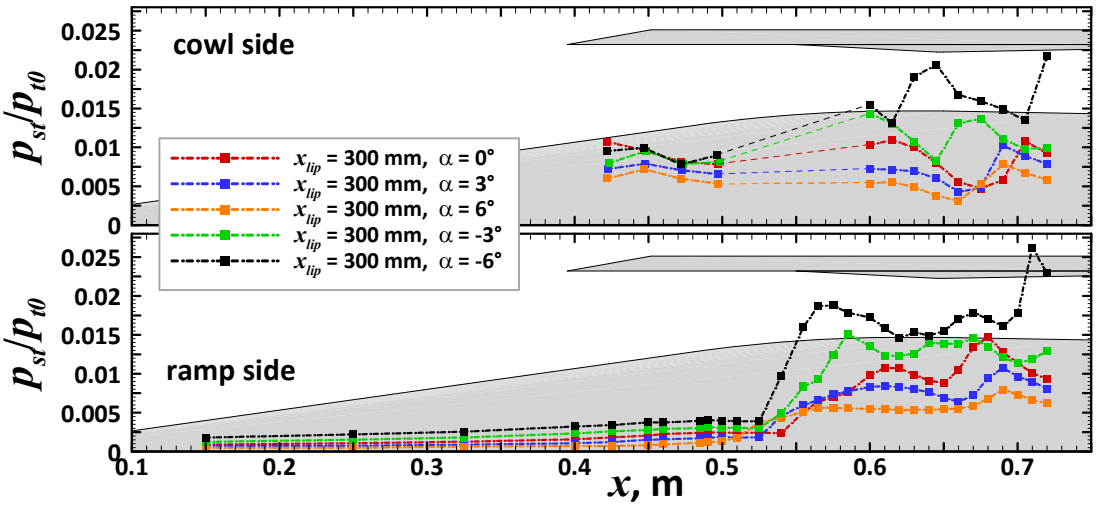

Figure 15: Static pressure distribution for different angles of attack for lip position of 300 mm

The wall pressure is strongly affected by α and is displayed in Figure 15. The patterns are consequent to the results of the pressure ratio and pressure recovery. For positive angle of attack, the shocks are weaker, and shock, resulting in smaller changes and overall lower pressure levels. The opposite can be observed for positive angles of attack. Furthermore, the shock angles are influenced as well, causing a shift of the shock structures in the streamwise direction. In the case of α = -6° the pressure peaks at the downstream end of both wall show that it has the effect that the shocks from the cowl lip and the beginning of the fixed part of the cowl are shifted so far upstream that they interact with the respective walls an additional time (as compared to the flow topology sketched in Figure 9). For other angles, the shift of the shock structure is also visible, but no as distinct.

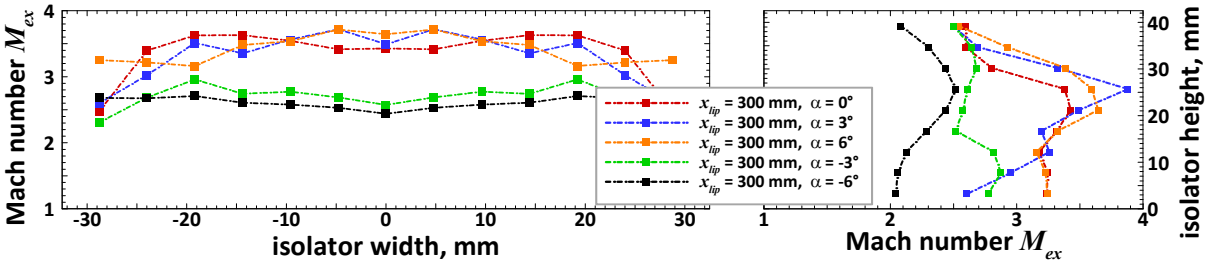

Figure 16: Mach number distributions for xlip = 300 mm with no backpressure applied

The vertical Mach number profiles in Figure 16 show the shift of any shock structures as well, noticeable by the jumps in the Mach number, although it is rather unsafe to conclude where each shock is located. In the cases of negative angle of attack, the Mach number at the isolator exit overall is considerably lower, especially for α = 6°, and the flow seems to be more uniform over both the spanwise and horizontal profile.

2. Angle of Yaw

Unlike with angle of attack, the angle of yaw was already set up before the start of the windtunnel run, meaning that the inlet has to start with the angle of yaw imposed on it. It should be noted here, that this can impact the results, as previous investigations showed that hysteresis effects can influence the results [49].

As Figure 17 shows, the total pressure losses are strongly increased by the angle of yaw, as the sidewall shock on the luv-ward side becomes much stronger. Except for the case of β = 6° and x_{lip} = 300 mm, however, there is no significant change to the static pressure ratio. It is interesting to note, that for β = 6°, there is a distinct difference between the two configurations, whereas for β = 3°, the results of both configurations are very similar. Regarding the performance at lower throttle degrees, the limit is at about the same throttle degree for all configurations, around Δ = 0.16. In the case of β = 6° the inlet appears to still be working at lower throttle degrees but was found to start buzzing at around this limit. For β = 3°, inlet buzz did not occur, the inlet operated stable up to the point of unstart.

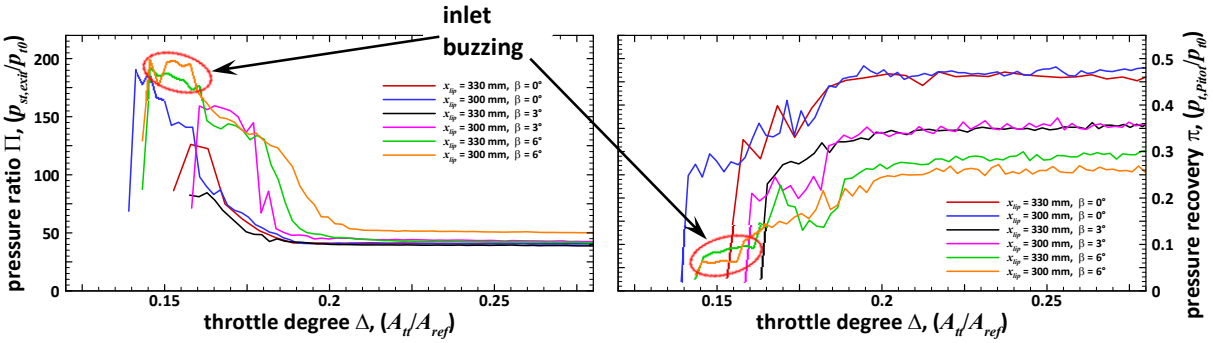

Figure 17: Static pressure ratio and total pressure recovery for different angles of yaw

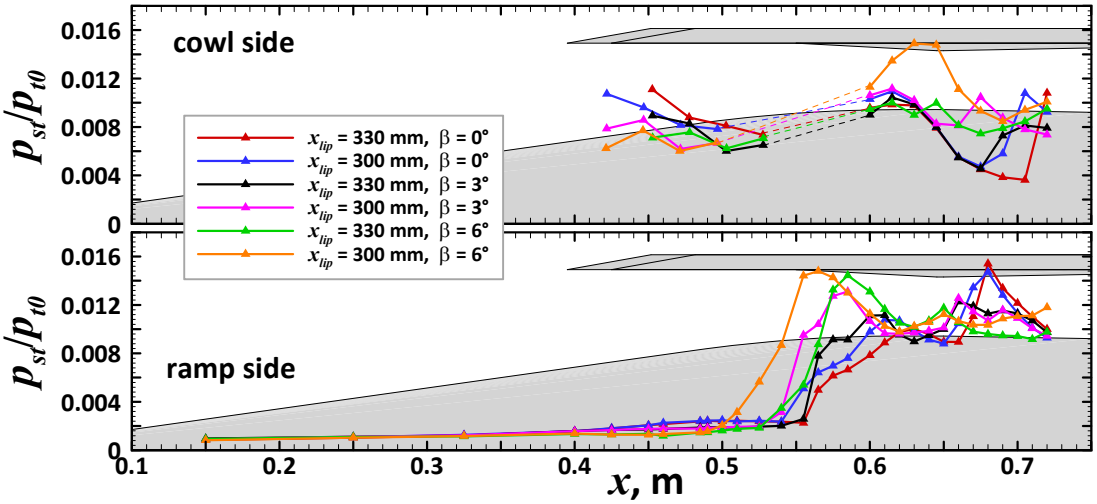

Figure 18: wall pressure distribution without backpressure for different angles of yaw

Figure 18 displays the wall pressure distribution for the different angles. The pressure peak on the ramp, at the interaction with the cowl shock, becomes significantly higher, when angle of yaw is applied (except for the case of x_{lip} = 330 mm and β = 3°). For β = 6° and x_{lip} = 6°, at the fixed part of the cowl, around x = 0.64 m, there is also a strong peak in static pressure which was not recorded for any of the other configurations. The pressure peaks marking the interaction of the shocks from the lip and the fixed part of the cowl in the case of β = 0° are not observed for any angle of yaw. Overall, if there is an angle of yaw, the changes in wall pressure in the downstream section of the isolator are smaller.

Surprisingly, the angle of yaw does not appear to introduce significant asymmetries to the flow. Only in the case of β = 3° and x_{lip} = 300 mm, a clear difference of the Mach number profile of both sides of the centerplane is noticeable. In contrast, the yaw angle has a strong influence on the vertical Mach number distribution. Especially in the case of β = 6°, the Mach number close to the bottom wall is much lower. This is probably due to the much stronger

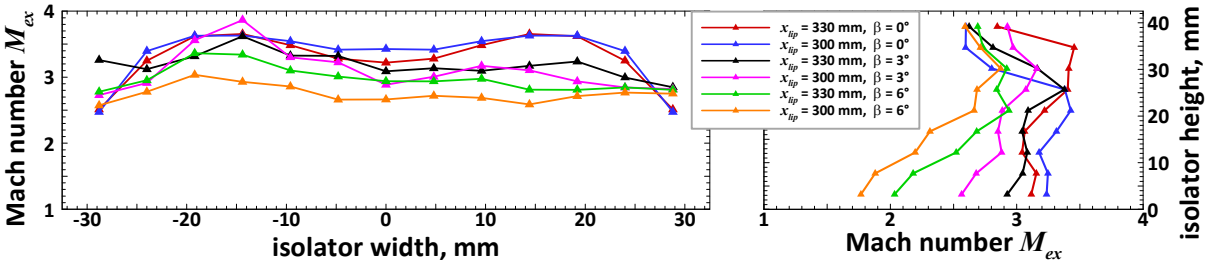

Figure 19: Mach number profiles for different angles of yaw

shock-boundary layer interaction of the lip shock with the ramp boundary layer, which was already noticed in the wall pressure.

Overall, it was observed that the flow field topology over the height of the isolator exit is strongly influenced by both angle of attack and angle of yaw. This could have a strong impact on fuel injection and mixing, and consequently the performance and stability of the combustion process.

Another aspect that is very important regarding the safe operation of the inlet is the mass capture. Angle of yaw and positive angle of attack decrease the capture area of the inlet, and, in the case of negative angle of attack, the mass capture can be lower as well. Although in this case, the capture area becomes higher, the higher ramp angle and consequent higher shock angle can lead to increased spillage. The changes of the mass capture, together with the performance parameters, of the experiments with flight path angles are listed in Table 3. Only in the case of $\alpha = 6°$, there is a significant reduction of the mass capture (up to 50%), the other configurations are not regarded critical where the MCR is decreased by only up to 25%. Note that the MCR = $\dot{m}_{ex}/\dot{m}_0$ always refers to reference mass flow $\dot{m}_0$ of the basic configuration with $\alpha = \beta = 0°$. Therefore, it is possible for some configurations to have an MCR > 1.

xlip, mm	α, °	β, °	MCR	πtot	Π_{st}	η_{ke}
300	0°	0°	0,97	0,47	41,58	0,98
	3°	0°	0,71	0,40	36,84	0,97
	6°	0°	0,51	0,33	27,17	0,96
	-3°	0°	0,94	0,31	62,33	0,96
	-6°	0°	1,09	0,28	86,89	0,95
	0°	3°	0,86	0,35	43,36	0,96
	0°	6°	0,84	0,26	50,90	0,95
330	0°	0°	0,92	0,45	42,79	0,97
	3°	0°	0,68	0,46	33,27	0,97
	6°	0°	0,47	0,33	25,84	0,96
	-3°	0°	0,91	0,34	50,94	0,96
	-6°	0°	1,05	0,28	77,49	0,95
	0°	3°	0,83	0,35	39,29	0,96
	0°	6°	0,77	0,29	42,32	0,96

Table 3: Overview of experiments with various flight path angles

D. Impact of Reynolds-Number

Another point that was examined is the influence of the Reynolds-Number on the flowfield. By changing Re, the different flight altitudes can be simulated. As already pointed out, the two test conditions are supposed to reproduce flights in 25 km and 30 km height. The influence of *Re* on the static pressure ratio and total pressure recovery for both the design configuration (x_{lip} = 330 mm) and maximum internal contraction (x_{lip} = 300 mm) are shown in Figure 20. Without applied backpressure the pressure ratio for both configurations is just slightly higher for the higher Re-number. The difference in pressure recovery is stronger for x_{lip} = 330 and 300 mm, with cond. 1 delivering higher values. For x_{lip} = 315 mm, there is no difference in the pressure recovery. At lower throttle degrees, the inlet operates more stable at cond. 1. As explained before, there are two distinct points up to which the inlet can operate depending on the lip position. For cond. 2, the inlet always unstarted at the same throttle degree of about Δ = 0.16.

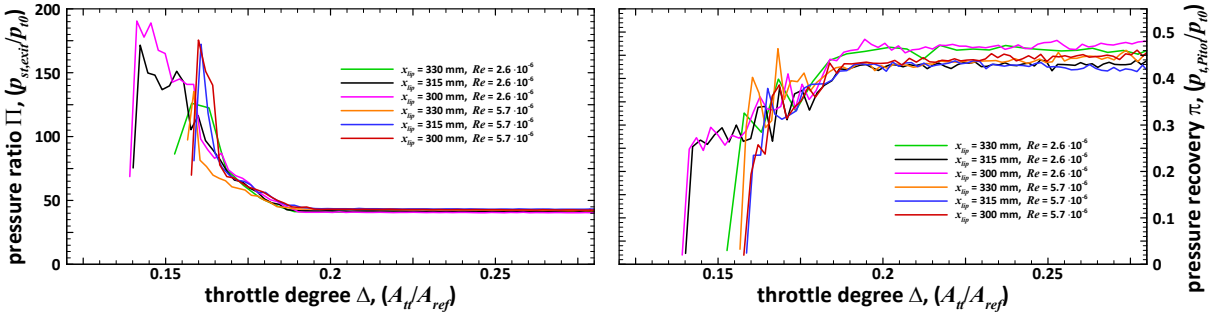

Figure 20: static pressure ratio and pressure recovery for different Reynolds numbers

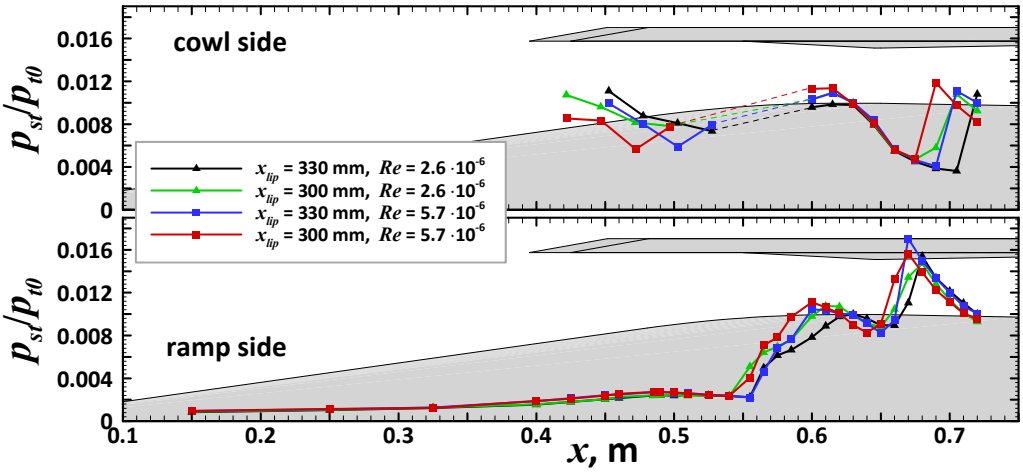

Figure 21: wall pressure distribution for different Reynolds-numbers for lip positions of 330 mm and 300 mm

Regarding the wall pressure distribution, there is significant Re-influence. Due to the impact on the boundary layer, especially close to the cowl lip, there is a shift in the shock structure, which is moved a bit upstream. However, the magnitude of the wall pressure is about the same for both conditions. An overview of the performance of the two conditions is given in Table 4.

Condition	xlip, mm	MCR	πtot	Π_{st}	η_{ke}
1	300	0,97	0,47	41,58	0,98
	315	0,95	0,42	41,56	0,97
	330	0,92	0,46	40,96	0,98
2	300	0,92	0,45	42,79	0,97
	315	0,91	0,43	43,32	0,97
	330	0,89	0,44	42,66	0,97

Table 4: Comparison of experiments with different Reynolds-numbers

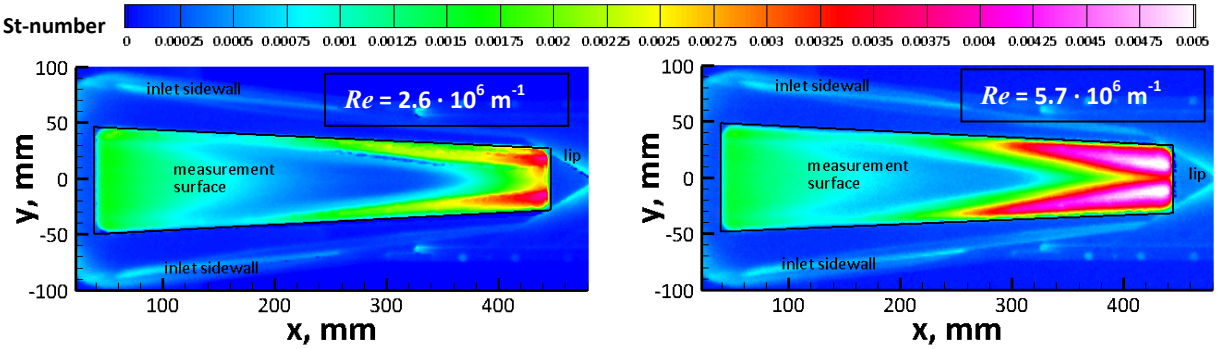

Figure 22: Stanton-number distribution on external ramp for different Reynolds numbers

Figure 22 shows the Stanton number distribution on the external ramp which was derived from the IR measurements. The images very well show the heating of the surface in the vicinity of the sidewall shocks. In the case of cond. 2, the maximum St-number is much higher than for the lower Re-number of cond. 1. Furthermore, the angle of the sidewall shocks for cond. 2 appears a little bit higher. This could be a result of the thicker boundary layer due to the higher Re-number. However, it has to be kept in mind that the results do not allow for a clear identification of the shock location. The results also show a clear asymmetry in the external flow field for both configurations. This is somewhat surprising as both the results from the pressure measurement rake as well as wall pressure measurements conducted around the perimeter of two cross-sections in the internal part did show a rather symmetric flow field.

V. Conclusion

The measurement campaign conducted with this 3D-inlet showed that it is well suited to satisfy all the requirements, although there are some several aspects that could not be investigated yet. The starting behavior fitted well with results from other 3D-inlets. During testing, the inlet operated most stable at the highest internal contraction ratio that was examined. It made a substantial difference, if the ramp shock went underneath the cowl. In the cases where this happened, the resulting flow structure was much more stable regarding operation at high backpressure ratios. Overall, the longer the internal section of the inlet was, the more resistant it was to inlet unstart caused by the backpressure. Increasing the Re-number led to less stable operation, as the point of inlet unstart shifted to higher throttle degrees. Furthermore, the heatloads on the external ramp was strongly increased.

The examination of flight path angles revealed, that the inlet still operated quite well for rather large angles of up to $\alpha = \pm 6°$ and $\beta = 6°$. Only for large positive angles of attack, and the resulting reduction of the capture area, the mass flow decreases significantly, so that safe operation would be in question, as the mass flow might not be sufficient anymore to ensure stable combustion. However, the pressure levels at the inlet exit are still high enough for supersonic combustion. The maximum pressure levels, at which the inlet still operated stable, was reduced in some cases, but not significantly. Overall, the results suggest that the inlet would be well fitted for the flight experiment that it was designed for.

Acknowledgements

We would like to thank the German Research Foundation DFG for their funding of this project within the frame of the research training group GRK 1095/2 “Aero-Thermodynamic Design of a Scramjet Propulsion System for Future Space Transportation Systems”. The contribution Institute of Material Science of the DLR, the provision of the material parameters of the thermoplastics used for the IR-measurements is also acknowledged. Further thanks to the operating team of the H2K windtunnel.

References

[1] W. H. Heiser and D. T. Pratt, “Hypersonic Airbreathing Propulsion”, 1st ed. Washington, D.C.: AIAA Education Series, 1994.

[2] R. S. Fry, “A Century of Ramjet Propulsion Technology Evolution,” *Journal of Propulsion and Power*, vol. 20, no. 1, pp. 27–58, 2004.

[3] M. K. Smart, N. E. Hass, and A. Paull, “Flight Data Analysis of the HyShot 2 Scramjet Flight Experiment,” *AIAA Journal*, vol. 44, no. 10, pp. 2366–2375, Oct. 2006.

[4] R. R. Boyce, S. C. Tirtey, L. Brown, M. Creagh, and H. Ogawa, “SCRAMSPACE : Scramjet-based Access-to-Space Systems,” *17th AIAA International Space Planes and Hypersonic Systems and Technologies Conference*, San Francisco, April 2011, AIAA 2011-2297.

[5] S. C. Tirtey, R. R. Boyce, L. M. Brown, and M. A. Creagh, “The SCRAMSPACE I Hypersonic Flight Experiment Feasibility Study,” *17th AIAA International Space Planes and Hypersonic Systems and Technologies Conference*, San Francisco, April 2011, AIAA 2011-2277.

[6] D. J. Dolvin, “Hypersonic International Flight Research and Experimentation (HIFiRE) - Fundamental Sciences and Technology Development Strategy,” *15th AIAA International Space Planes and Hypersonic Systems and Technologies Conference*, Dayton, Ohio, April 2008, AIAA 2008-2581.

[7] R. L. Kimmel, D. Adamczak, D. Dolvin, M. Borg, and S. Stanfield, “Aerothermodynamic Insight from the HIFiRE Program,” *Proceedings of the 7th European Symposium on Aerothermodynamics for Space Vehicles*, Brugge, Belgium, May 2011, ESA SP-692.

[8] C. Mcclinton, V. Rausch, R. Shaw, U. Metha, and C. Naftel, “Hyper-X: Foundation for future hypersonic launch vehicles,” *Acta Astronautica*, vol. 57, pp. 614–622, Jul. 2005.

[9] C. R. Mcclinton, V. L. Rausch, L. T. Nguyen, and J. R. Sitz, “Preliminary X-43 flight test results,” *Acta Astronautica*, vol. 57, pp. 266–276, Jul. 2005.

[10] J. M. Hank, J. S. Murphy, and R. C. Mutzman, “The X-51A Scramjet Engine Flight Demonstration Program,” *15th AIAA International Space Planes and Hypersonic Systems and Technologies Conference*, Dayton, Ohio, May 2008, AIAA 2008-2540.

[11] J. Steelant, "LAPCAT : High-Speed Propulsion Technology," *Advances on Propulsion Technology for High-Speed Aircraft*, NATO Research and Technology Organization, Neuilly-sur-Seine, France, 2008, RTO-EN-AVT-150, Paper 12, pp. 12–1 – 12–38.

[12] J. Steelant, "Sustained Hypersonic Flight in Europe: Technology Drivers for LAPCAT II," *16th AIAA/DLR/DGLR International Space Planes and Hypersonic Systems and Technologies Conference*, Bremen, Germany, November 2009, AIAA 2009-7240.

[13] F. Falempin and L. Serre, "LEA Flight Test Program," *11th AIAA/AAAF International Space Planes and Hypersonics Systems and Technologies Conference*, Orléans, France, 2002, AIAA 2002-5249.

[14] F. Falempin and L. Serre, "LEA flight test program - a first step to an operational application of high-speed airbreathing propulsion," *12th AIAA International Space Planes and Hypersonic Systems and Technologies*, Norfolk, Virginia, December 2003, AIAA 2003-7031.

[15] U. Gaisbauer, B. Weigand, B. U. Reinartz, H.-P. Kau, and W. Schröder, "Research Training Group GKR 1095/1: Aero-Thermodynamic Design of a Scramjet Propulsion System," *18th International Symposium on Airbreathing Engines (ISABE)*, Beijing, China, September 2007, Paper 2007-1131.

[16] B. Weigand and U. Gaisbauer, "An Overview on the Structure and Work of the DFG Research Training Group GRK 1095: Aero-Thermodynamic Design of a Scramjet Propulsion System," *16th AIAA/DLR/DGLR International Space Planes and Hypersonic Systems and Technologies Conference*, Bremen, Germany, November 2009, AIAA 2009-7276.

[17] D. M. van Wie, "Scramjet Inlets," Scramjet Propulsion, *Progress in Astronautics and Aeronautics,* vol. 189, American Institute of Aeronautics and Astronautics, Reston, Virginia, 2000, ISBN 1-56347-322-4, pp. 447 – 511.

[18] S. D. Holland, "Reynolds Number and Cowl Position Effects for a Generic Sidewall Compression Scramjet Inlet at Mach10: A Computational and Experimental Investigation," *AIAA 17th Aerospace Ground Testing Conference*, Nachville, Tennessee, July 1992, AIAA 1992-4026.

[19] S. D. Holland and K. J. Murphy, "An Experimental Parametric Study of Geometric, Reynolds Number, and Ratio of Specific Heats Effects in Three-Dimensional Sidewall Compression Scramjet Inlets at Mach 6," *31st AIAA Aerospace Sciences Meeting and Exhibit*, Reno, Nevada, 1993 AIAA 1993-0740.

[20] S. D. Holland, "Mach 10 Experimental Database of a Three-Dimensional Scramjet Inlet Flow Field," NASA Technical Memorandum, NASA TM-4648, 1995.

[21] E. H. Andrews, C. R. Mcclinton, and S. Z. Pinckney, "Flow Field and Starting Characteristics of an Axisymmetric Mixed Compression Inlet," NASA Technical Memorandum, NASA TM X-2072, 1971.

[22] D. M. V. Wie and D. A. Aultt, "Internal Flowfield Characteristics of a Scramjet Inlet at Mach 10," *Journal of Propulsion and Power*, vol. 12, no. 1, pp. 158–164, 1996.

[23] K. Triesch, "Ebener Scramjeteinlauf SCR1 (Aufbau der Innenströmung und Einfluss der Einspritzelemente)," DLR Interner Bericht, DLR IB 39113 – 2000 C 03, 2000.

[24] B. Decoene and A. Henckels, "Untersuchung eines Einlaufmodells im Hyperschallkanal H2K des DLR," DLR Interner Bericht, DLR IB – 39113 – 2001A15, 2001.

[25] R. T. Voland, L. D. Huebner, and C. R. Mcclinton, "X-43A Hypersonic vehicle technology development," *Acta Astronautica*, vol. 59, pp. 181–191, Jul. 2006.

[26] P. Gruhn, "Inviscid design of the inlet for the LAPCAT Mach 8 configuration," DLR Interner Bericht, DLR IB 32418 – 2006A28, 2006.

[27] J. Häberle and A. Gülhan, "Investigation of Two-Dimensional Scramjet Inlet Flowfield at Mach 7," *Journal of Propulsion and Power*, vol. 24, no. 3, pp. 446–459, 2008.

[28] F. S. Billig and A. P. Kothari, "Streamline Tracing : Technique for Designing Hypersonic Vehicles*," Journal of Propulsion and Power*, vol. 16, no. 3, pp. 465–471, 2000.

[29] M. K. Smart, "Design of Three-Dimensional Hypersonic Inlets with Rectangular-to-Elliptical Shape Transition," *Journal of Propulsion and Power*, vol. 15, no. 3, pp. 408–416, May 1999.

[30] T. F. O'Brien, "Viscous Performance Map of a Blunt Streamline-Traced Busemann Inlet," *17th AIAA International Space Planes and Hypersonic Systems and Technologies Conference*, San Francisco, April 2011, AIAA 2011-2255.

[31] J. Riehmer, Personal Correspondence, 2010.

[32] M. C. Banica, T. Scheuermann, J. Chun, B. Weigand, and J. von Wolfersdorf, "Numerical Study of Supersonic Combustion Processes with Central Strut Injection," *Journal of Propulsion and Power*, vol. 26, no. 4, pp. 869–874, Jul. 2010.

[33] B. U. Reinartz and U. Gaisbauer, "Numerical Investigation of 3D Intake Flow," *17th AIAA International Space Planes and Hypersonic Systems and Technologies Conference*, San Francisco, April 2011, AIAA 2011-2351.

[34] O. Dessornes and D. Scherrer, "Tests of the JAPHAR dual mode ramjet engine," *Aerospace Science and Technology*, vol. 9, no. 3, pp. 211–221, Apr. 2005.

[35] M. K. Smart, "How Much Compression Should a Scramjet Inlet Do?," *AIAA Journal*, vol. 50, no. 3, pp. 610–619, Mar. 2012.

[36] Y. P. Goonko, A. F. Latypov, I. I. Mazhul, A. M. Kharitonov, M. I. Yaroslavtsev, and P. Rostand, "Structure of Flow over a Hypersonic Inlet with Side Compression Wedges," *AIAA Journal*, vol. 41, no. 3, pp. 436–447, Mar. 2003.

[37] T. Nguyen, M. Behr, B. U. Reinartz, O. Hohn, and G. Ali, "Numerical Investigations of the Effects of Sidewall Compression and Relaminarization in 3D Scramjet Inlet," *17th AIAA International Space Planes and Hypersonic Systems and Technologies Conference*, San Francisco, April 2011,AIAA 2011-2256.

[38] O. M. Hohn and A. Gülhan, "Experimental Investigation on the Influence of Sidewall Compression on the Flowfield of a Scramjet Inlet at Mach 7," *17th AIAA International Space Planes and Hypersonic Systems and Technologies Conference*, San Francisco, April 2011, AIAA 2011-2350.

[39] A. Kantrowitz and C. duP. Donaldson, "Preliminary Investigation of Supersonic Diffusers," NACA Wartime Report, NACA ACR No. L5D20, 1945.

[40] B. Sun and K. Zhang, "Empirical Equation for Self-Starting Limit of Supersonic Inlets," *Journal of Propulsion and Power Technical Notes*, vol. 26, no. 4, pp. 874 – 875, Mar. 2010.

[41] C. A. Trexler, "Inlet Starting Predictions for Sidewall-Compression Scramjet Inlets," *24th AIAA/SAE/ASME/ASEE Joint Propulsion Conference*, Boston, Massachusetts, July 1988, AIAA 1988-3257.

[42] X. Veillard, R. Tahir, E. Timofeev, and S. Mölder, "Limiting Contractions for Starting Simple Ramp-Type Scramjet Intakes with Overboard Spillage," *Journal of Propulsion and Power*, vol. 24, no. 5, pp. 1042–1049, Sep. 2008.

[43] F.-J. Niezgodka, "Der Hyperschallwindkanal H2K des DLR in Köln-Porz (Stand 2000)," DLR Mitteilung 2001–01, 2001.

[44] A. M. O. Smith and A. B. Bauer, "Static-Pressure Probes that are Theoretically Insensitive to Pitch, Yaw and Mach Number," *Journal of Fluid Mechanics*, vol. 44, no. 3, pp. 513–528, 1970.

[45] S. Z. Pinckney, "An Improved Static Probe Design," *AIAA Journal*, vol. 12, no. 4, pp. 562–564, Apr. 1974.

[46] S. Z. Pinckney, "Short Static-Pressure Probe Design for Supersonic Flow," NASA Technical Note, NASA TN-D-7978, 1975.

[47] J. D. Anderson jr., Modern Compressible Flow with Historical Perspective, 3rd ed. New York, NY, USA: McGraw-Hill, ISBN 007-124136-1, 2004.

[48] "Pressure Systems 8400 Users Manual," 1991.

[49] O. M. Hohn and A. Gülhan, "Experimental Investigation on the Influence of Yaw Angle on the Inlet Performance at Mach 7," *48th AIAA Aerospace Sciences Meeting and Exposition*, Orlando, Florida, January 2010, AIAA 2010-938.

[50] J. Häberle, "Untersuchungen zum externen und internen Strömungsfeld eines Scramjet Triebwerkseinlaufs bei unterschiedlichen Betriebspunkten," DLR Forschungsbericht, ISRN DLR-FB—2009-14, 2009.

[51] K. Triesch and E.-O. Krohn, "Verwendung von Kegeldüsen zur Drosselung und Durchsatzmessung bei Überschalleinläufen," DLR Interner Bericht, DLR IB-39113-83-A-04, 1984.

[52] "DIN 1952 - Durchflussmessung mit Blenden, Düsen und Venturirohren in voll durchströmten Rohren mit Kreisquerschnitt," Beuth Verlag, Berlin, 1982.

[53] Flir Systems, "ThermaCam SC-3000 Users Manual," Portland, OR, 1999.

[54] A. Henckels and P. Gruhn, "Study on Aerothermal Effects of Viscous Shock Interaction in Hypersonic Inlets," *Proceedings of the Fifth European Symposium on Aerothermodynamics for Space Vehicles*, Cologne, Germany, November 2005, ESA SP-563.